TECHNICAL PAPER

Prototyping of absorber plate for solar collector by ISF and FSW processes

Rafael Gustavo Schreiber[1] · Andrison Rodrigues Teixeira[2] · Rafael Santiago Floriani Pereira[1] · Fernando da Silva Osório[1] · Lirio Schaeffer[2]

Abstract

The absorber plates in solar energy collectors are usually manufactured using copper pipes welded or pressed to aluminum sheets. This paper presents the development of an innovative model of absorber plate for flat plate solar collector using the incremental sheet forming (ISF) and the friction stir welding (FSW) processes. This absorber plate is formed and welded symmetrically using two 1 mm thick AA1200-H14 aluminum sheets, as to allow water ducts to be formed between them. In order to determine the ISF parameters, six groove test experiments were conducted varying tool diameter and step-down value. The results of the groove test were compared with those obtained by finite element simulation. To determine the FSW parameters, four experiments were conducted varying the feed rate. Following that, a flat plate solar collector absorber plate prototype was manufactured. Based on the results, it is believed that the proposed approach seems to be effective to manufacture solar collector absorber plate prototypes using the ISF and FSW processes. The ducts were manufactured by ISF until the final thickness determined in the project (0.48 mm) without sheet cracking. It was also possible to carry out the FSW process of joints without defects identified in the bending test, however, some improvements are necessary to guarantee the tightness of the joint.

Keywords ISF · FSW · Solar collector · Prototyping

1 Introduction

Commercial solar collectors are commonly used to heat water at a temperature range between 50 and 70 °C for domestic and industrial purposes [1, 2]. These products are usually constituted of welded copper pipes with heat absorber plates mounted on them [3]. The copper pipes, through which the water passes to be heated, are mounted in a thermally isolated box with glass on top. The manufacturing of this type of collector requires extensive manual pipe welding operations with subsequent fins mounted onto them.

In this study, we analyzed the viability of manufacturing a new solar collector model where, instead of copper pipes, two aluminum sheets would be formed symmetrically. After forming, the sheets would be welded together creating a duct to allow water passage (Fig. 1). In order to achieve this, a solar collector prototype was manufactured to include a top sheet and a bottom sheet using the incremental sheet forming (ISF) process. Afterward, the friction stir welding (FSW) process was used to join the sheets together.

✉ Rafael Gustavo Schreiber
   rafael.schreiber@ifsc.edu.br

   Andrison Rodrigues Teixeira
   andrison@g1equipamentos.com.br

   Rafael Santiago Floriani Pereira
   rsfpereira@gmail.com

   Fernando da Silva Osório
   fernando.osorio@ifsc.edu.br

   Lirio Schaeffer
   schaefer@ufrgs.br

1 Federal Institute of Education, Science and Technology of Santa Catarina (IFSC), Lages, SC 88506-400, Brazil

2 Federal University of Rio Grande Do Sul (UFRGS), Porto Alegre, RS 91501-970, Brazil

🙂 Springer
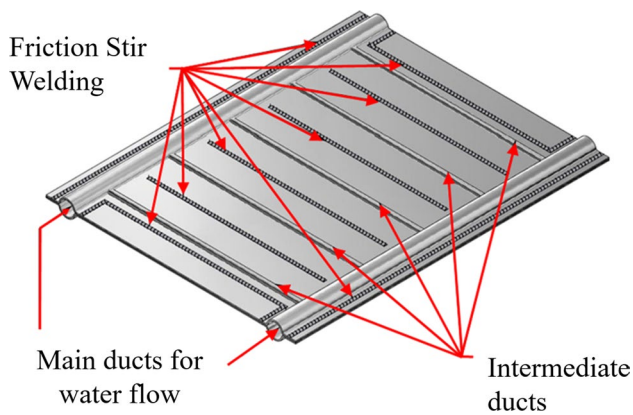
Fig. 1 New solar collector model

This model had its patent application sent to the National Institute of Industrial Property (INPI) under the code BR102017024107-6. Its main advantage is that its manufacturing methods that can be easily automated. However, as previously stated, it needs to be mounted in a thermally insulated box with glass on top (not shown in Fig. 1). In this new model, similarly to commercial solar collectors, water is heated as it passes through the main and intermediary ducts.

The ISF process was applied for quick prototyping. Since it does not require expensive tools in comparison to conventional stamping [4], this allowed the tool path to determine the piece's final shape [5], and it can easily be made using a CNC production center [6, 7]. In this process, the sheet is fixated at the extremities, while a semi-spherical tipped tool, in rotation speed, moves against it as the tool path determines the shape [8]. This process improves formability compared to conventional stamping [9, 10]. However, the sheet's limited geometric precision after ISF forming is still a major obstacle for industrial implementation [11].

The FSW process has since been applied in a series of materials with applications in the maritime, rail, automotive, aeronautics and aerospace industries [12]. In the FSW, a rotating tool is plunged in the joint interface, due to the amount of heat generated due to friction with the base material, plastic deformation is induced, resulting in the union in the solid state [13, 14]. It is possible to apply the FSW to butt joints, lap joints, fillet joints and other joints [15, 16]. In the FSW thin plate process, weld thinning is a problem that may compromise the joint's integrity and mechanical properties [17]. The plunge depth needs to be controlled to prevent joint

thickness reduction and excessive flash [18]. In addition, this reduction in thickness and strength of the joint after welding is influenced by rotation and tool speed parameters [18, 19]. Microhardness, tensile strength and wear properties in aluminum alloys joined by FSW can be increased by addition of reinforcement nanoparticles [14, 20–24].

2 Materials and methods

The experimental procedure was divided into three stages: the first consists on the ISF groove test, the second on the finite element simulation of the ISF groove test, and the third on the friction stir welding experiments.

In the three stages, the materials used in the experiments were 1 mm thick AA1200-H14 aluminum sheets. This material was selected for the solar collector prototype for its high thermal conductivity (222 W/mK). Table 1 presents the material's main properties.
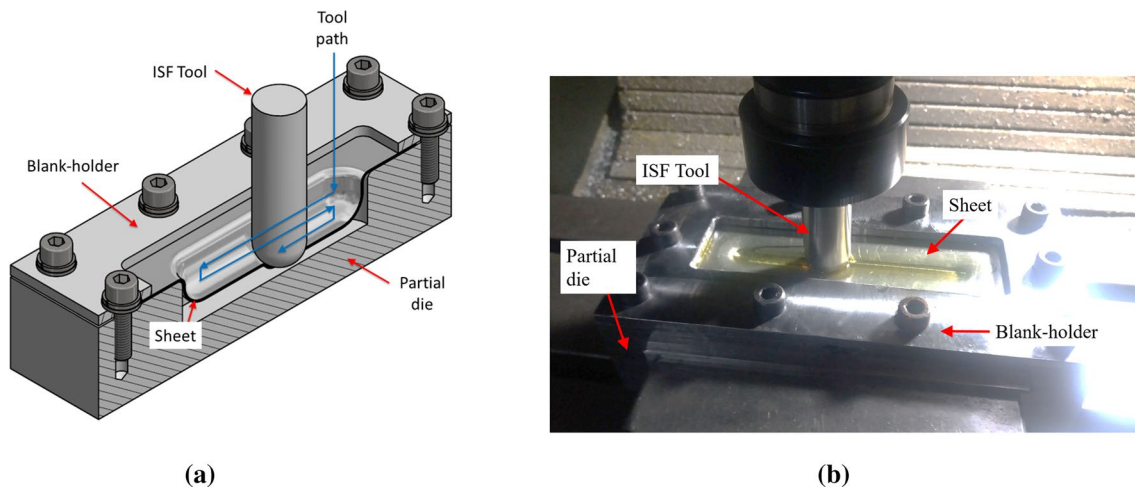
2.1 ISF experiments

Six grove test experiments were conducted to define the incremental sheet forming parameters in order to manufacture the solar collector prototype. In these experiments, 100 mm long grooves were formed onto a 1 mm thick AA1200-H14 aluminum sheet, fixated between a blank-holder and a partial die, with the tool path defined as shown in Fig. 2a, which presents the set's isometric sectional view. In the experiments, the tool followed a vertical path forming the plate to a defined step-down value, followed by a horizontal path (100 mm path), and a new vertical path with a defined step-down. This course was repeated successively until a plate fracture occurred, indicating the major strain of the sheet for the selected parameters.

The experiments were conducted using a Romi CNC production center model Discovery 308, with travel X of 450 mm, travel Y of 310 mm and travel Z of 410 mm. The rotation speed was kept at $S = 50$ rpm, and the feed rate at $F = 250$ mm/min. These parameters were selected based on the Schreiber and Schaeffer [25] studies. The experiments were conducted until the first crack in the sheet was identified, registering the maximum tool depth h as indicated on the CNC production center panel.

The variable parameters in each experiment were the step-down of $\Delta z = 2$ mm, 1 mm and 0.5 mm, and the tool

Table 1 AA1200-H14 properties

Yield strength (MPa)	Tensile strength (MPa)	Elongation (%)	Modulus of elasticity (GPa)	Yield constant, C (MPa)	Strain-hardening exponent, n (−)	Roughness Ra (μm)
97	117	3.6	70	181.45	0.108	0.50

Fig. 2 **a** Isometric sectional view of the configuration used in the ISF experiments, **b** ISF process being performed at the CNC production center

diameters of d_t 22 mm and 9.5 mm (the same diameters of the prototype's main duct and intermediary duct).

The ISF tools were manufactured with high-speed steel, and ISO VG 100 oil was used for lubrication in all experiments. Figure 2b shows the ISF manufacturing process with a 22 mm diameter tool at the CNC production center.

2.2 FEM simulation

Finite element method (FEM) was conducted to validate the results obtained in the ISF experiments. With FEM simulation, the values of major strain, minor strain and thickness strain, obtained at tool depth h, before fracture identification, were also evaluated.

The FEM simulation was performed using the Simufact Forming software in the Sheet Metal Forming module, in the 3D simulation type and with element type solid. The tool, the blank-holder, the partial die and the sheet were modeled to perform the groove test of each experiment. However, to decrease the simulation time, the channel length was decreased in the simulation model.

The tool paths were configured by table (tabular motion) using the time calculated for each path as a tool feed rate function in the experiments (250 mm/min). The contact table was configured in the "glued" option between sheet and blank-holder, and in the "touching" option for other contacts. The initial temperature of the partial die and the tool were set at 20 °C. The friction coefficient selected was 0.1 following Coulomb's law.

The sheet material was configured as AA1200-H14 with a flow curve of $\sigma_F = 181.45\ \varphi^{0.108}$. The material was considered isotopic in the simulation. The sheet mesh was created with element edge length of 1.0 mm and with 3 elements over thickness. Hexahedron elements were selected for meshing the sheet blank. The first level of refinement was defined for the

refinement box indicated in Fig. 3, with dimensions defined according to groove size.

For the incremental sheet forming, the strain limits were defined by the fracture forming limit diagram (FFLD), represented by a descending line on the φ_1 and φ_2 axis, in which thickness strain φ_3 is constant, resulting in a -1 slope. From the limit strain data obtained in the FEM simulation and using the law of volume constancy (Eq. 1), it was possible to define the value of major strain for the plane strain conditions (Eq. 2) and the value of major strain for the state of equal bi-axial stretching (Eq. 3), and thus build the FFLD for each experiment.

$$\varphi_1 + \varphi_2 + \varphi_3 = 0 \tag{1}$$

$$\varphi_{1\text{plane}} = -\varphi_3 \tag{2}$$

$$\varphi_{1\text{bi - axial}} = \varphi_{2\text{bi - axial}} = -\frac{\varphi_3}{2} \tag{3}$$
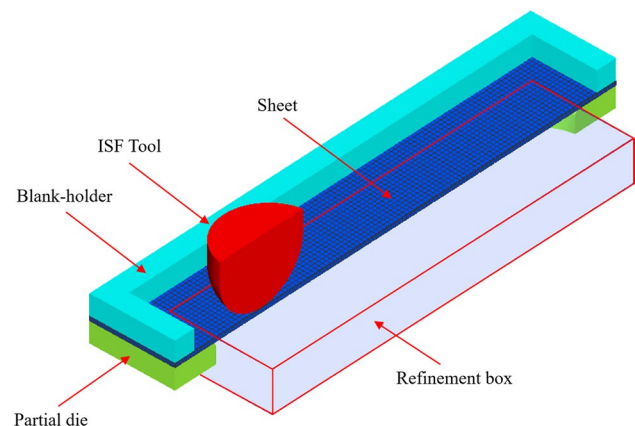
Fig. 3 Assembly of ISF groove test to FEM

The thickness strain φ_3 can be determined as a function of initial thickness s_0 and the final thickness s, using Eq. 4. Isolating the final thickness in Eq. 4, it is possible to determine its value through Eq. 5. This final thickness is considered the critical value, the one in which the strain occurs on the sheet within the ISF parameters used.

$$\varphi_3 = \ln\left(\frac{s}{s_0}\right) \tag{4}$$

$$s = s_0\, e^{\varphi_3} \tag{5}$$

2.3 FSW experiments

Four experiments were performed to define the friction stir welding parameters to be used in the solar collector prototype manufacturing. In these experiments, 1 mm thick aluminum AA1200-H14 sheet lap joints were welded together, fixed between a blank-holder and a backing plate. In this process, the shoulder tool kept the 0.1 mm plunge depth, holding a 0.4 mm distance at the joint bottom, without tool inclination, as indicated in Fig. 4. The 0.4 mm length has been selected so as not to pierce the bottom surface of the joint [26].
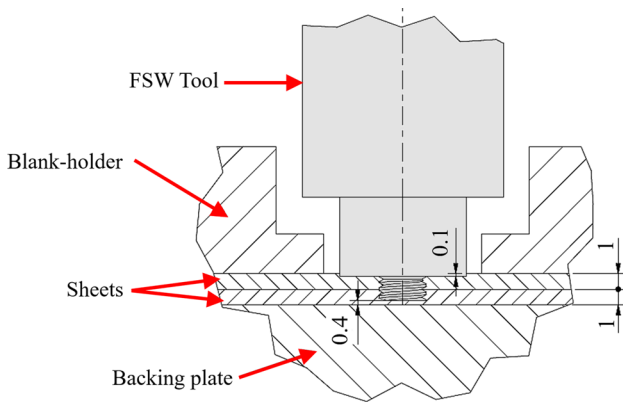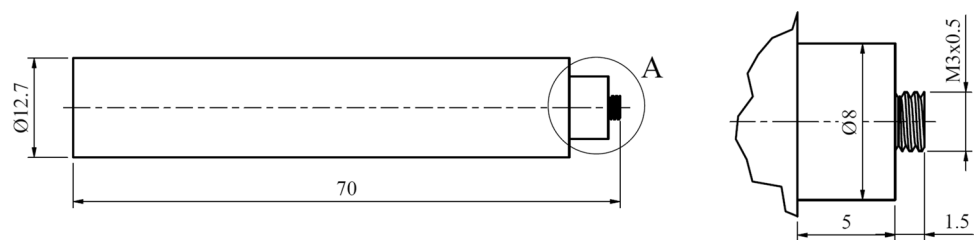

Fig. 4 Configuration used in FSW experiments

Fig. 5 FSW tool design

DETAIL A

The FSW tool was projected with an 8 mm diameter shoulder and an M3×0.5 threaded pin, as indicated in Fig. 5. The tool was made with VC 131 tool steel.

Each experiment was performed with a different feed rate value ($F = 100$ mm/min, 200 mm/min, 300 mm/min and 400 mm/min), while tool rotation was kept at $S = 1500$ rpm. In each experiment, two overlapping aluminum sheets with dimensions 1 mm × 250 mm × 360 mm were welded together. To ensure correct fixing of the sheets, it was necessary to drill holes in them to assemble the blank-holder. The holes were positioned far enough away from the joint so as not to interfere with the quality of the weld, as shown in Fig. 6.

After the welding, cuts were made to provide four specimens for bend test and four specimens for macrography (Fig. 6). Following the ISO/DIS 25239-4 norm recommendations, the initial and final 50 mm around the welded regions were disconsidered in the specimens' sections used for bend test and for macrography.

The experiments were performed in a Romi CNC production center model Discovery 308 (the same used in the ISF experiments). Figure 7 presents a photograph of the lap joint during welding, which indicates a flash being formed due to tool shoulder penetration into the joint after the FSW tool passed through. That process required a later operation to remove the flash.

For each welded joint, four specimens were cut for bend test. The cuts were made using wire erosion (two to be bent at the weld's root and two to be bent at the weld's face). The bend test was conducted with a 10 mm radius punch bending and a 26 mm cavity base, up to the 180° bend angle and according to the NBR ISO 7438 norm. This test was performed in an INSTRON/EMIC Universal Test Machine model EMIC 23–600, with a capacity of 600 kN.

3 Results and discussion

3.1 Influence of ISF parameters

After six ISF experiments with tool diameter of $d_t = 22$ mm and 9.5 mm, and step-down value of $\Delta z = 2$ mm, 1 mm and

Fig. 6 Specimens for FSW experiments
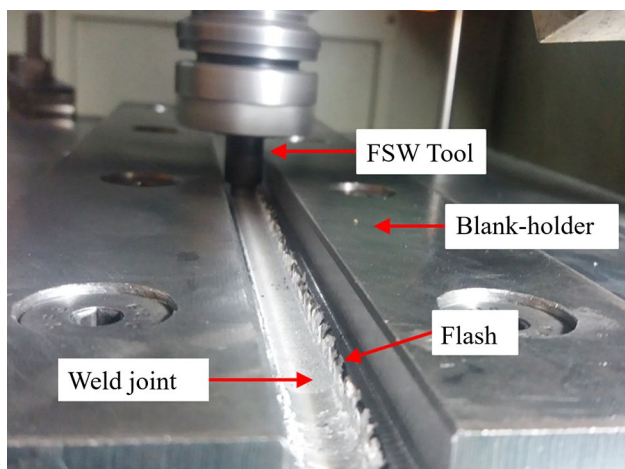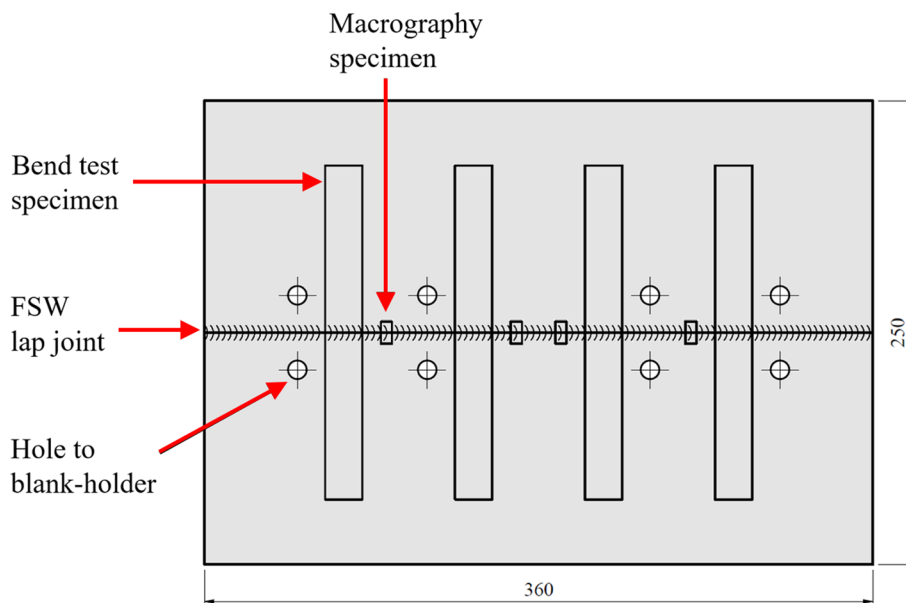
Fig. 7 FSW process being performed at the CNC production center

center before cracks were identified. In the FEM simulation, strain values were determined in the place where sheet thickness was at its lowest.

Even though greater formed depths were achieved with tool diameter at 22 mm ($h = 8$ to 10 mm), the greatest strains were obtained with a 9.5 mm tool diameter ($\varphi_3 = -1.12$ to -1.58). Figure 8 shows photographs of the six experiments indicating at each line the tool diameter, and in each column the step-down value. The places where the strains first occurred and where the experiment was interrupted are also indicated in this figure.

It is also possible to see in Fig. 8 that with the step-down at $\Delta z = 2$ mm the crack occurred catastrophically no matter the diameter size used. As the step-down decreased, it was possible to obtain greater strains and the fracture only occurred at the formed groove's extremity.

As such, through the FEM Simulation, we were able to confirm the experimental results, which indicated that the critical region in the groove test occurs at the extremities where lower thickness were obtained, as shown in Fig. 9. The end of the groove is a critical point in this test, as it

0.5 mm, the maximum formed depth (h), the sheet final thickness (s) and the strains (φ_1, φ_2 e φ_3) were verified as indicated below in Table 2. The h values were obtained by the tool depth value indicated by the CNC production

Table 2 ISF groove test results

No	d_t	Δz	h	s	φ_1	φ_2	φ_3
	(mm)	(mm)	(mm)	(mm)	(-)	(-)	(-)
1	22.0	2.0	8.0	0.56	0.46	0.12	−0.61
2	22.0	1.0	10.0	0.36	0.73	0.30	−1.03
3	22.0	0.5	10.0	0.36	0.73	0.30	−1.03
4	9.5	2.0	6.0	0.33	0.88	0.24	−1.12
5	9.5	1.0	6.0	0.33	0.88	0.24	−1.12
6	9.5	0.5	6.5	0.21	1.18	0.40	−1.58

**Fig. 8** ISF experiments cracks starting points
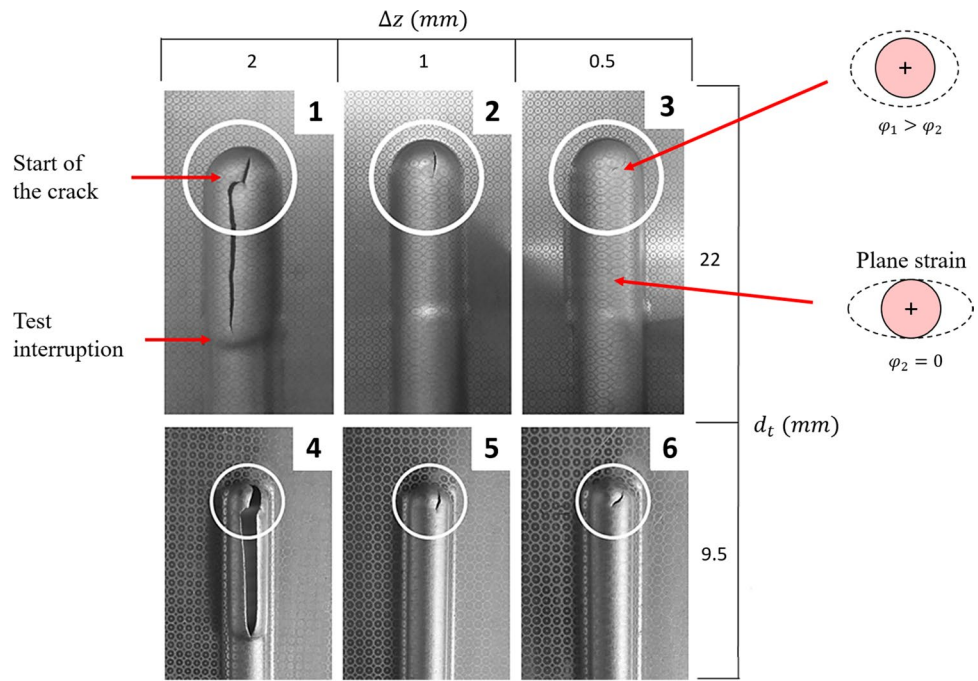
presents greater triaxiality, so it is the site that will present the crack first [25].

Figure 10 shows the FFLD obtained from each ISF experiment. In these experiments, it is evident that greater formability was obtained in the groove test with a 9.5 mm diameter tool compared to the 22 mm diameter tool. This result is in agreement with the literature, which indicates that greater deformations in ISF can be obtained with a smaller tool diameter [27]. In studies carried out by Kumar et al. [28], tool diameter is the most significant parameter in formability, followed by step-down. According to Martins et al. [25], the greater conformability obtained with a small tool diameter can be attributed to the triaxiality in the process (σ_m/σ_{eq}). Increasing the diameter of the tool also increases

the triaxiality, making the process similar to conventional stamping, with less formability.

In the studies of Al-Ghamdi and Hussain [29], it was verified that the maximum formability in ISF is reached with stable deformation, which can be obtained by a relation between the tool radius r_t and the initial thickness of the plate s_0, following the rule $r_t \approx 2.2\ s_0$. Using a tool radius above or below this limit value, formability is reduced.

In Fig. 10, it is clear that the decrease in step-down value allows for greater strains, as was seen in studies by Zhang et al. [30] and in studies by Schreiber and Schaeffer [25]. This result is consistent with the studies by Silva et al. [31], which indicates that low step-down values reduce the stresses in the process, resulting in greater conformability.
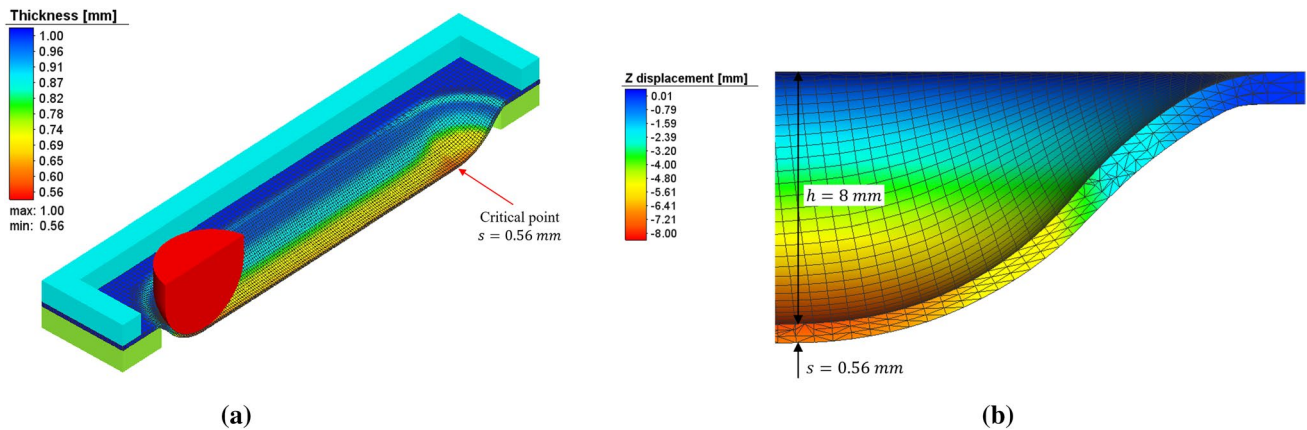
Fig. 9 **a** Isometric sectional view of results in FEM to first groove test (thickness), **b** Front section of critical point (Z displacement)

Fig. 10 FFLD for each ISF groove test
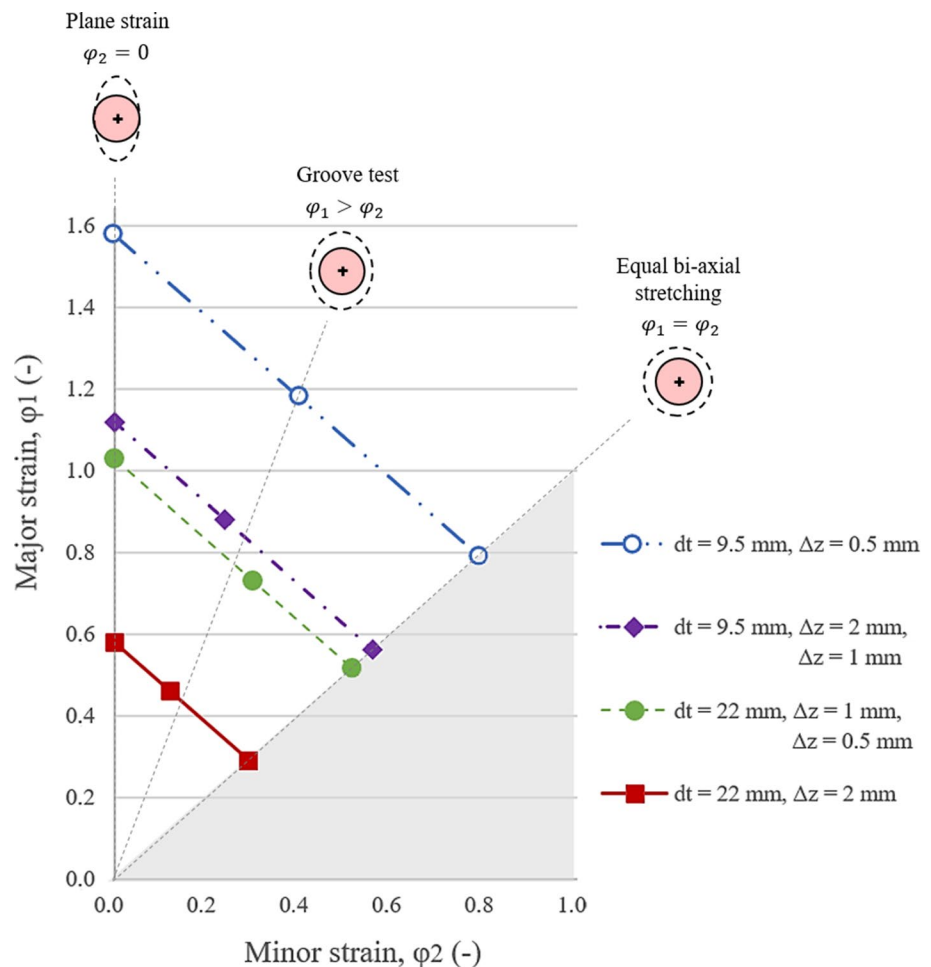
However, it should be noted that low step-down values result in an increase of the time required to manufacture the part [32, 33].

To manufacture the prototype, it was necessary to obtain $\varphi_3 = -0.73$ ($s = 0.48$ mm) for the main duct and $\varphi_3 = -0.63$ ($s = 0.53$ mm) for the intermediate duct in plane strain conditions. Using the shortest manufacturing time as a criterion, these strains can be obtained with $d_t = 22$ and $\Delta z = 1$ mm for the main duct, and with $d_t = 9.5$ and $\Delta z = 2$ mm for the intermediate duct.

3.2 Influence of FSW parameters

Face and root bend tests were conducted after uniting the lap joints through FSW with different tool feed rates. Using visual inspection, it was verified that no void defects or strains occurred in the bent specimens, both internally and externally, even after achieving an 180º bending angle. Figure 11 presents a photograph of the face and root bends for each feed rate used in the experiments. It also shows an amplified detail of the welding done in the fourth experiment.

The fact that the welded joint quality was not affected by the feed rate indicates that a higher feed rate ($F = 400$ mm/min) can be used to manufacture the prototype, allowing for the welding to be done in less time.

During this study, in preliminary tests without weld tool plunge depth, it was possible to verify a void defect, as indicated in the macrograph in the upper part of Fig. 12, where AS refers to Advancing Side and RS to Retreating Side.

When welding lap joints, it is possible to encounter a void defect, which presents itself as a hollow area in the welded region, as indicated by Arruda et al. [34], for welding lap joints of pure aluminum sheets with thickness 1 mm. In the studies by Chen et al. [35], for weld lap joints of 2A12-T4 aluminum alloy sheets with 2 mm thickness, the plunge depth was varied in a range of 0.13 mm until it was possible to verify the o remove of the void defect.

In addition, as indicated by Sahu and Pal [36], to weld AM20 magnesium alloy butt joints 4 mm thick, with plunge depth ranging from 0.03 to 0.21 mm, the best mechanical properties of tensile strength, bending, and microhardness were obtained with an intermediate plunge depth of 0.12 mm. Huang et al. [18] obtained the best quality welding

Fig. 11 FSW specimens after bend test

DATAIL VIEW
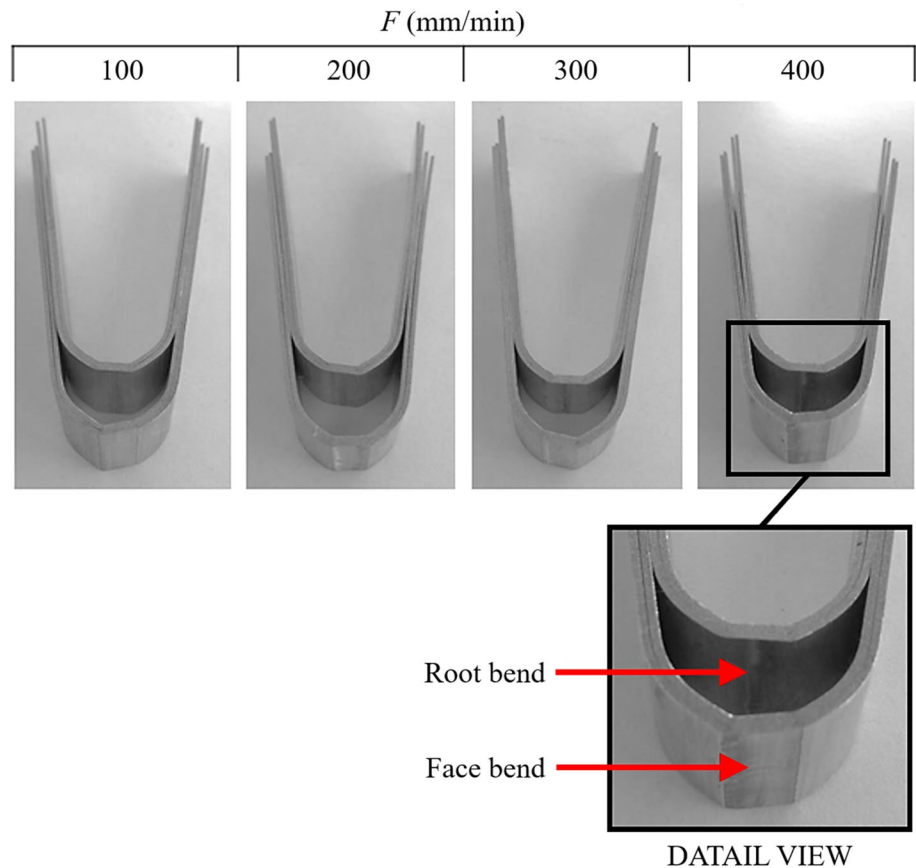
of thin Al-6061 sheets with 0.5 mm thickness using a plunge depth of 0.05 mm.

In this work, with a 0.1 mm plunge depth it was possible to reduce defect size in welded joints. However, a flash was produced in the process. Figure 12 shows the macrographs of welded joints at 100 to 400 mm/min feed rate (welded joints at 100 to 300 mm/min speeds are shown after flash removal). These samples are presented after attack by immersion using 10 g of NaOH and 90 ml of distilled water over a period of 60 s at 70 °C, followed by cleansing using distilled water.

All welded joints (at speeds between 100 and 400 mm/min) with Fig. 12's plunge depth showed significant flash and 0.1 mm roughing. In all experiments, the material was shifted from Retreating Side to Advancing Side, where you can see the junction of the sheets. However, with a feed rate of 100 mm/min, the sheets' union region was very limited and had an irregularity in the lower left. In the welded joint with 200 mm/min feed rate, the union region is larger, but there are discontinuities in its central area. With a 300 mm/min feed rate, besides the central area discontinuities, discontinuity also appears in the lower left region. And with a 400 mm/min feed rate, however, the union region is more homogeneous, even though it has a small discontinuity in the lower region.

Although all welded joints with 100 to 400 mm/min feed rates showed good results after bending test, based on the cross-section macrographs, it is possible to state that the feed rate value of 400 mm/min provided the greatest homogeneity joint and the smallest discontinuity extension.

Other alternatives could be explored in order to obtain more satisfactory results, such as the use of triple helix shoulder and tapered pin tools [37], the increase of the feed rate window and the analysis of other rotation speeds, as well as the decrease of plunge depth to avoid roughing the welded joint and to reduce flash [18, 19].
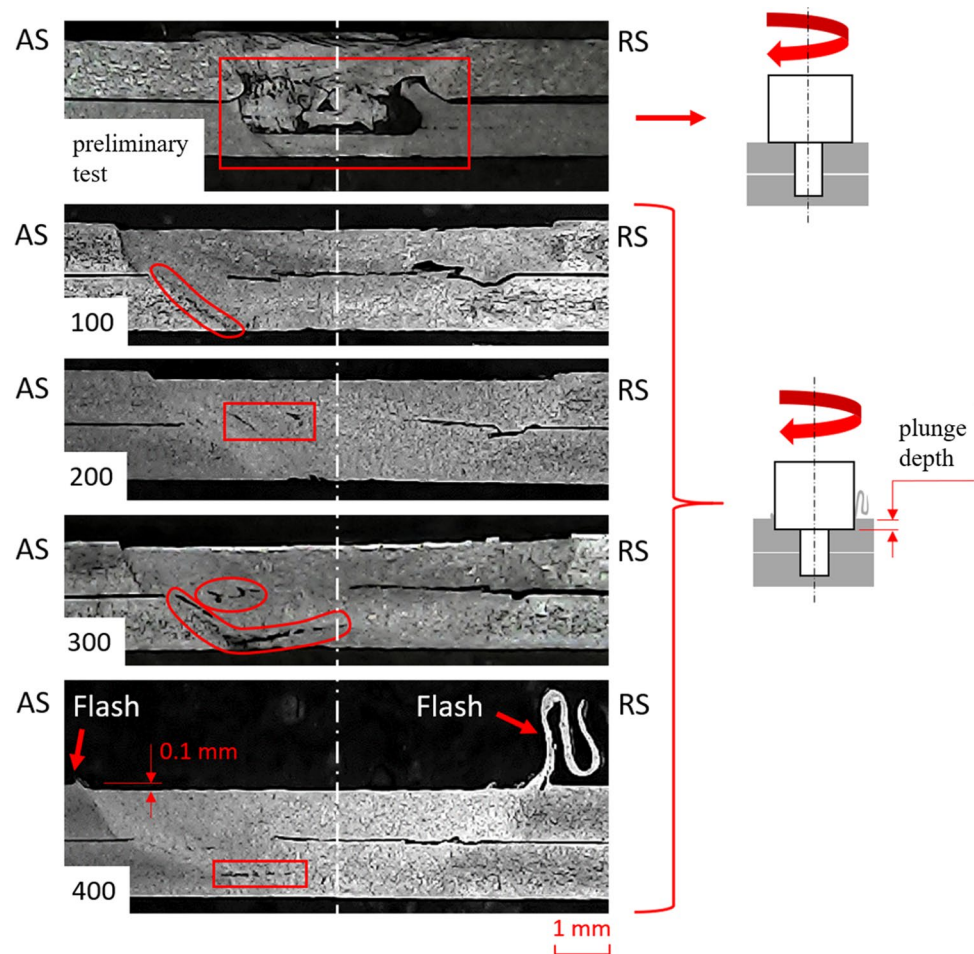
3.3 Manufacturing the prototype

The ISF and FSW parameters were selected to manufacture the solar collector prototype absorber plates since these processes allowed for manufacturing in a shorter period of time without compromising the product's quality. This prototype was designed from specifications for commercial collector's pipes, with main ducts with 22 mm in diameter and intermediary ducts with 9.5 mm in diameter. The prototype's total absorbent area was defined at 0.12 m^2 (315 mm × 380 mm).

It was necessary to use a device made of a polymeric die (polyacetal) and a SAE 1020 steel blank-holder for both processes. Polymeric holders and steel supporters were also

Fig. 12 Macrostructures in FSW cross section

used to stop the sheet from warping during the process. Figure 13 presents an exploded view of the device used in the prototype manufacturing.

The incremental sheet forming with a 22 mm tool diameter and a step-down value of $\Delta z = 1$ mm was used to create the main duct, since this parameter presented greater forming depth during shorter process time in the experiments conducted. With these parameters, it was possible to manufacture the main duct while meeting the condition of a plane strain with $\varphi_3 = -0.73$ (in the depth $h = 11$ mm) without cracks in the duct region. However, at the conformed extremities, where strain conditions were not plane, cracks occurred. Nevertheless, this did not compromise the prototype since the main grooves' extremities were cut through machining after forming the sheet.

For intermediary ducts, a 9.5 mm tool diameter and a step-down value of $\Delta z = 2$ mm were used, since the require depth was $h = 4.75$ mm with $\varphi_3 = -0.63$ in plane strain conditions. However, in the first stage, the tool step-down value was of 0.75 mm, and in the other stages a 2 mm step-down was used in order to obtain total groove depth of 4.75 mm without cracks in the duct region.
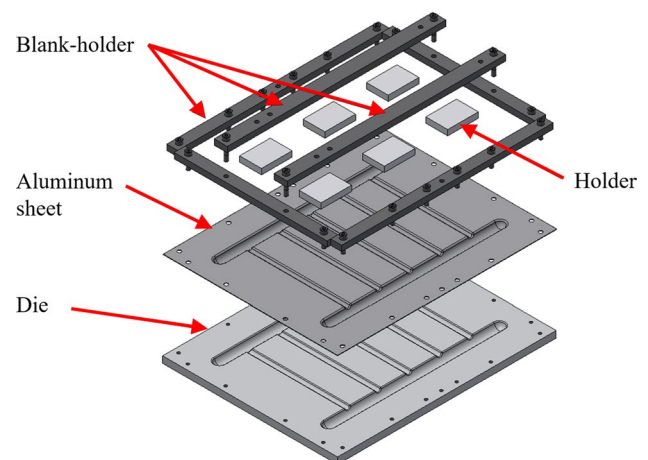
Fig. 13 Exploded view of sheet assembly for prototype manufacturing

Since the tool feed rate did not influence welded joint quality throughout the FSW process, the feed rate that presented the greatest value in the tests was selected

($F = 400$ mm/min) as to allow for prototype manufacturing at the shortest period of time.

To weld joints positioned between the prototype's intermediary grooves, it was necessary to previously drill a hole with 2.5 mm in diameter and 1.7 mm in depth at the position, facilitating the FSW tool's plunge depth penetration over the joint.

During the welding process, it was also verified that the use of intermediary supports was not enough to ensure the welded joint's regularity. Flash was not generated in the whole tool path, and the prototype's bead finish was not regular.

After welding the absorber plate, the set's outline was cut. This cut was made using a milling process at the same CNC production center, using a 6 mm diameter end mill. After that, the absorber plate went through a painting process with matte black spray paint (a common process in solar collectors in order to increase the product's efficiency). Figure 14a presents the absorber plate after being cut and painted, indicating the location of the welded joints. Figure 14b presents an absorber plate indicating the water ducts.

After the prototype was manufactured, the tightness test was performed according to NBR 15747-2: Solar thermal systems and their components—Solar Collectors Part 2:

Test Methods. For this test, it was necessary to assemble copper tubes with 22 mm outside diameter in the prototype inlet and outlet connections.

To perform the tightness test, as shown in Fig. 15, a hydraulic pump was installed at the system inlet and the fluid was driven by a hose connected to a ball valve. After that, copper tubes led the fluid to the manifold, passing through a pressure gauge. At the system outlet, another ball valve was installed to seal it after the air leaked. Welded copper tubes closed the other collector connection points. To weld copper–copper and aluminum-copper, a gas welding Zincaflux brazing rod (with an Zn and Al alloy) was used.

During the tightness test, after hydraulic pressure was released and air escaped, leaks were found at the locations indicated in Fig. 15. These leak locations are at the welded joints' starting points, located between the intermediate ducts. In these regions, previous drilling was performed for the FSW tool plunge depth penetration, which facilitated welding, but compromised joint tightness. This indicates that for it to be possible to manufacture this new collector model it would be necessary to evaluate other possibilities regarding the implementation of the weld bead without previously drilling a hole at the site.

Fig. 14 a FSW locations on prototype, **b** water ducts for prototype
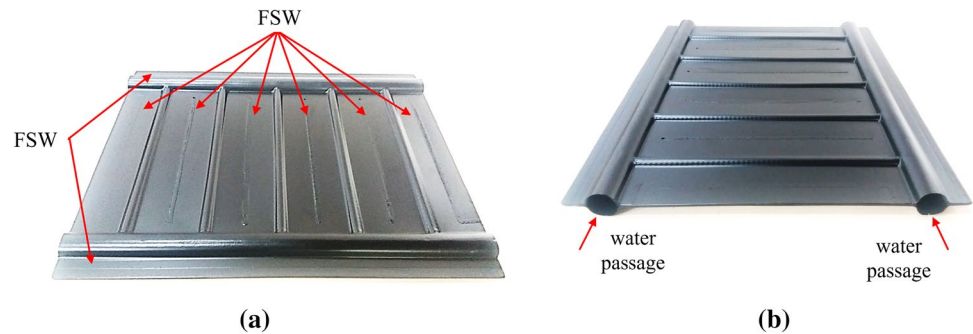
Fig. 15 Tightness test
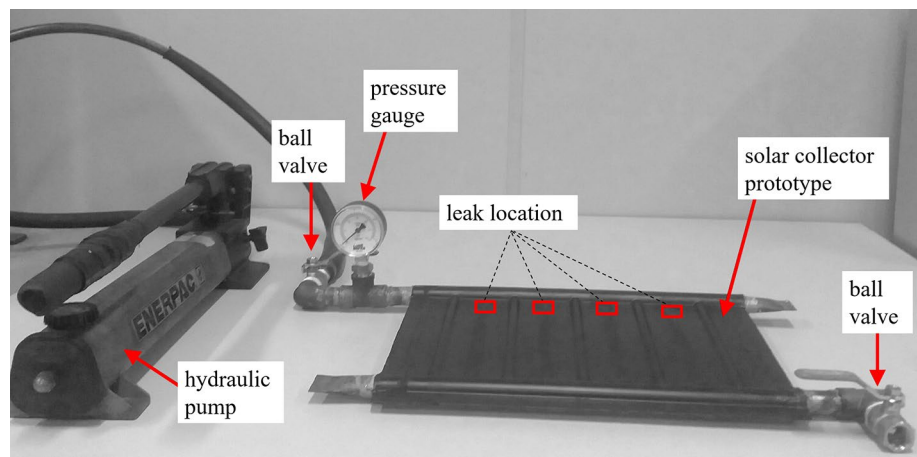
4 Conclusions

This study presented a new alternative for construction and manufacturing processes applied to flat plate solar collectors' absorber plates. After conducting ISF and FSW experiments and manufacturing the product's prototype, it was possible to obtain the following conclusions:

1. The FEM simulation combined with the ISF groove test enabled a satisfactory FFLD prediction for each parameter range, which was decisive for the selection of the prototype's manufacturing parameters: $\Delta z = 2$ mm for intermediate ducts and $\Delta z = 1$ mm for main ducts;
2. The intermediate ducts of the collector prototype were shaped by ISF until the final thickness of 0.53 mm, while the main ducts were shaped up to a thickness of 0.48 mm, according to the design, without crack of the sheet;
3. Using rotation speed 1500 rpm and feed rate of 100 to 400 mm/min, it was possible to weld joints by FSW, which did not present defects in the bending test;
4. The best result for weld lap joints using FSW was obtained using a 400 mm/min feed rate. In this condition, the weld became more homogeneous and the process was carried out in a shorter period of time;
5. The use of plunge depth of 0.1 mm in the FSW process was crucial to avoid the void defect, reducing discontinuities in the lap joint;
6. It is possible to manufacture solar collector absorber plate prototypes using ISF and FSW processes. However, it is necessary to develop a suitable method to implement the FSW process in the middle of the plate without compromising joint tightness.

Compliance with ethical standards

References

1. Khan MMA, Ibrahim NI, Mahbubul IM et al (2018) Evaluation of solar collector designs with integrated latent heat thermal energy storage: a review. Sol Energy 166:334–350. https://doi.org/10.1016/j.solener.2018.03.014
2. Pandey KM, Chaurasiya R (2017) A review on analysis and development of solar flat plate collector. Renew Sustain Energy Rev 67:641–650. https://doi.org/10.1016/j.rser.2016.09.078
3. Palacio M, Rincón A, Carmona M (2020) Experimental comparative analysis of a flat plate solar collector with and without PCM. Sol Energy 206:708–721. https://doi.org/10.1016/j.solener.2020.06.047
4. Shrivastava P, Tandon P (2019) Microstructure and texture based analysis of forming behavior and deformation mechanism of AA1050 sheet during Single Point Incremental Forming. J Mater Process Technol 266:292–310. https://doi.org/10.1016/j.jmatprotec.2018.11.012
5. Li Y, Daniel WJT, Meehan PA (2017) Deformation analysis in single-point incremental forming through finite element simulation. Int J Adv Manuf Technol 88:255–267. https://doi.org/10.1007/s00170-016-8727-9
6. Peng W, Ou H, Becker A (2019) Double-sided incremental forming: a review. J Manuf Sci Eng. https://doi.org/10.1115/1.4043173
7. Mohanty S, Regalla SP, Rao YVD (2019) Influence of process parameters on surface roughness and forming time of Al-1100 sheet in incremental sheet metal forming. J Mech Eng Sci 13:4911–4927. https://doi.org/10.15282/jmes.13.2.2019.11.0408
8. Jiménez I, López C, Martinez-Romero O et al (2017) Investigation of residual stress distribution in single point incremental forming of aluminum parts by X-ray diffraction technique. Int J Adv Manuf Technol 91:2571–2580. https://doi.org/10.1007/s00170-016-9952-y
9. Dwivedy M, Kalluri V (2019) The effect of process parameters on forming forces in single point incremental forming. Proced Manuf 29:120–128. https://doi.org/10.1016/j.promfg.2019.02.116
10. Ai S, Long H (2019) A review on material fracture mechanism in incremental sheet forming. Int J Adv Manuf Technol. https://doi.org/10.1007/s00170-019-03682-6
11. Ren H, Xie J, Liao S et al (2019) In-situ springback compensation in incremental sheet forming. CIRP Ann 68:317–320. https://doi.org/10.1016/j.cirp.2019.04.042
12. Gite RA, Loharkar PK, Shimpi R (2019) Friction stir welding parameters and application: a review. Mater Today Proc 19:361–365. https://doi.org/10.1016/j.matpr.2019.07.613
13. Shah LH, Walbridge S, Gerlich A (2019) Tool eccentricity in friction stir welding: a comprehensive review. Sci Technol Weld Join 24:566–578. https://doi.org/10.1080/13621718.2019.1573010
14. Singh T, Tiwari SK, Shukla DK (2020) Effect of nano-sized particles on grain structure and mechanical behavior of friction stir welded Al-nanocomposites. Proc Inst Mech Eng Part L J Mater Des Appl 234:274–290. https://doi.org/10.1177/1464420719885156
15. Singh K, Singh G, Singh H (2018) Review on friction stir welding of magnesium alloys. J Magnes Alloy 6:399–416. https://doi.org/10.1016/j.jma.2018.06.001
16. Kumar M, Das A, Ballav R (2020) Influence of interlayer on microstructure and mechanical properties of friction stir welded dissimilar joints: a review. Mater Today Proc 26:2123–2129. https://doi.org/10.1016/j.matpr.2020.02.458
17. Guan M, Wang Y, Huang Y et al (2019) Non-weld-thinning friction stir welding. Mater Lett 255:126506. https://doi.org/10.1016/j.matlet.2019.126506
18. Huang Y, Meng X, Zhang Y et al (2017) Micro friction stir welding of ultra-thin Al-6061 sheets. J Mater Process Technol 250:313–319. https://doi.org/10.1016/j.jmatprotec.2017.07.031
19. Huang Y, Meng X, Lv Z et al (2019) Microstructures and mechanical properties of micro friction stir welding (μFSW) of 6061–T4 aluminum alloy. J Mater Res Technol 8:1084–1091. https://doi.org/10.1016/j.jmrt.2017.10.010
20. Singh T, Tiwari SK, Shukla DK (2019) Friction-stir welding of AA6061-T6: the effects of Al2O3 nano-particles addition. Results Mater 1:100005. https://doi.org/10.1016/j.rinma.2019.100005

21. Singh T, Tiwari SK, Shukla DK (2020) Effects of Al_2O_3 nanoparticles volume fractions on microstructural and mechanical characteristics of friction stir welded nanocomposites. Nanocomposites 6:76–84. https://doi.org/10.1080/20550324.2020.1776504

22. Tanvir Singh SK, Tiwari DKS (2021) Influence of nanoparticle addition (TiO_2) on microstructural evolution and mechanical properties of friction stir welded AA6061-T6 joints. Adv Prod Ind Eng. https://doi.org/10.1007/978-981-15-5519-0_18

23. Singh T, Tiwari SK, Shukla DK (2020) Mechanical and microstructural characterization of friction stir welded AA6061-T6 joints reinforced with nano-sized particles. Mater Charact 159:110047. https://doi.org/10.1016/j.matchar.2019.110047

24. Singh T, Tiwari SK, Shukla DK (2020) Novel method of nanoparticle addition for friction stir welding of aluminium alloy. Adv Mater Process Technol. https://doi.org/10.1080/2374068X.2020.1855397

25. Schreiber RG, Schaeffer L (2019) Manufacture of absorber fins for solar collector using incremental sheet forming. J Mater Res Technol 8(1):1132–1140. https://doi.org/10.1016/j.jmrt.2018.07.018

26. Khan NZ, Siddiquee AN, Khan ZA (2018) Proposing a new relation for selecting tool pin length in friction stir welding process. Meas J Int Meas Confed 129:112–118. https://doi.org/10.1016/j.measurement.2018.07.015

27. Gatea S, Lu B, Chen J et al (2019) Investigation of the effect of forming parameters in incremental sheet forming using a micromechanics based damage model. Int J Mater Form 12:553–574. https://doi.org/10.1007/s12289-018-1434-3

28. Kumar N, Singh A, Agrawal A (2020) Formability analysis of AA1200 H14 aluminum alloy using single point incremental forming process. Trans Indian Inst Met 73:1975–1984. https://doi.org/10.1007/s12666-020-02014-7

29. Al-Ghamdi KA, Hussain G (2015) Threshold tool-radius condition maximizing the formability in SPIF considering a variety of materials: experimental and FE investigations. Int J Mach Tools Manuf 88:82–94. https://doi.org/10.1016/j.ijmachtools.2014.09.005

30. Zhang S, Tang GH, Wang W, Jiang X (2020) Evaluation and optimization on the formability of an AZ31B Mg alloy during warm incremental sheet forming assisted with oil bath heating. Meas J Int Meas Confed 157:107673. https://doi.org/10.1016/j.measurement.2020.107673

31. Ham M, Jeswiet J (2006) Single point incremental forming and the forming criteria for AA3003. CIRP Ann Manuf Technol 55:241–244. https://doi.org/10.1016/S0007-8506(07)60407-7

32. Centeno G, Bagudanch I, Martínez-Donaire AJ et al (2014) Critical analysis of necking and fracture limit strains and forming forces in single-point incremental forming. Mater Des 63:20–29. https://doi.org/10.1016/j.matdes.2014.05.066

33. Rauch M, Hascoet JY, Hamann JC, Plenel Y (2009) Tool path programming optimization for incremental sheet forming applications. CAD Comput Aided Des 41:877–885. https://doi.org/10.1016/j.cad.2009.06.006

34. de Arruda RP, Baroni A, Schaeffer L (2008) Sheet metal forming: new technologies applied to the fabrication of solar energy collector panels. Int J Mechatronics Manuf Syst 1:254–263. https://doi.org/10.1504/IJMMS.2008.02051

35. Chen D, Li J, Zhao H et al (2020) Effect of submillimeter variation in plunge depth on microstructure and mechanical properties of FSLW 2A12 aluminum alloy joints. Acta Metall Sin (English Lett) 33:165–171. https://doi.org/10.1007/s40195-019-00981-5

36. Sahu PK, Pal S (2018) Effect of FSW parameters on microstructure and mechanical properties of AM20 welds. Mater Manuf Process 33:288–298. https://doi.org/10.1080/10426914.2017.1279295

37. Liu F, Fu L, Chen H (2018) High speed friction stir welding of ultra-thin AA6061-T6 sheets using different backing plates. J Manuf Process 33:219–227. https://doi.org/10.1016/j.jmapro.2018.05.020